

# THERMAL HYDRAULIC ANALYSIS IN REACTOR VESSEL INTERNALS CONSIDERING IRRADIATION HEAT

**Sungje Hong, Kunwoo Yi, Jin Huh, Inyoung Im and Eunkee Kim**

KEPCO Engineering and Construction Company, INC.

NSSS Division, KEPCO E&C, Inc, 989-111 Daeduckdaero, Yuseong-gu, Daejeon, Korea

[sjhong@kepco-enc.com](mailto:sjhong@kepco-enc.com); [kwyi@kepco-enc.com](mailto:kwyi@kepco-enc.com); [jhuh@kepco-enc.com](mailto:jhuh@kepco-enc.com);

[iyim@kepco-enc.com](mailto:iyim@kepco-enc.com); [ekkim2@kepco-enc.com](mailto:ekkim2@kepco-enc.com)

## ABSTRACT

The present study is to evaluate flow and temperature distributions in the APR1400 reactor vessel internals (RVIs) considering irradiation heat using the computational fluid dynamics code. The analysis is performed using a simplified reactor core model and the one-quarter geometry model that is postulated to be the flow symmetry condition, to calculate more effectively. The axial power density at the beginning of cycle (BOC), middle of cycle (MOC) and end of cycle (EOC) conditions is used as inputs to the CFD analysis, and velocity and temperature distributions are calculated on the four cross-sections of the reactor vessel (RV): lower support structure (LSS), core shroud (CS), upper part of the core and hot/cold leg center line. This method established the effect of a variation of the flow according to BOC, MOC and EOC conditions. The results of each model show the similar patterns in the flow distributions, however, the little difference appears in the temperature distributions under the operating conditions. The results of CFD analysis for the surface temperature distributions on the internals can be used for boundary conditions to perform stress analysis of the reactor vessel internals for the APR1400.

## KEYWORDS

IASCC, CFD, Internals, BOC, MOC, EOC

## 1. INTRODUCTION

The APR1400 reactor vessel internals (RVI) consists of two major structures, as the core support structures and internal structures. Their role is to assure the integrity of the core by providing direct support, restraint, envelope for the core, etc. Most of the RVI components are made of stainless steel Type 304 and jointed by the stainless steel Type 308L or 347 welds.

The RVI of APR1400 operates in harsh conditions, such as long term exposure to neutron irradiation, high temperatures, reactor water environment, and other operating loads. Even though they are mainly made of Type 304 austenitic stainless steel which is well known to have good mechanical properties and corrosion resistance, these operating conditions, especially neutron irradiation, cause them to age, which is characterized by a chromium depletion along grain boundaries of austenitic stainless steel, decrease in ductility and fracture toughness of the steel, increase in yield and ultimate strength of the steel, and cause potential volume change due to void formation in the steel[1-2]. Although initially viewed as a completely independent, IASCC is now seen as an accelerant of the environmental cracking processes, stress corrosion cracking (SCC). Radiation causes decomposition of water into many species which affect the corrosion potential and especially the presence of fast neutron irradiation, which has a stronger effect on water chemistry, acts to enhance the process of SCC[3].

Recently, Electric Power Research Institute, Inc. (EPRI) started the researches on aging management for pressurized water reactor internals and published several material reliability programs (MRPs) to provide the guidelines for the evaluation and aging management methodologies and procedures for operating RVI, especially for the reactors whose lives were extended to 60 years. Even though the MRPs have a purpose to provide the evaluation or management methodologies for the operating RVI, the similar evaluation methodologies can be applied to the APR1400 fleet in the design stage for the evaluation of neutron irradiation effects on their RVI design.

In this study, Computational fluid dynamics (CFD) analysis techniques are applied in order to get the necessary data, in all regions inside the APR1400 reactor assembly and quantitatively and systematically understand the heat flow phenomena in the fluid flowing condition considering irradiation heat, which could be used as the boundary condition for an analysis for IASCC and void swelling.

## 2. NUMERICAL SIMULATION

### 2.1. Configuration of Geometric Model

The internal structures of the RVI are all structures within the RV other than the core support structures, fuel assemblies, control element assemblies (CEA) and instrumentation. The general arrangement of the APR1400 reactor are shown in Figure 1.

The major structural member of the RVI is the CSB assembly. The CSB assembly consists of the CSB, the lower support structure (LSS) and In-Core Instrumentation (ICI) nozzle assembly, and the core shroud.

In carrying the heat flow analysis in the internal shape, there is difficulty in directly transferring a complete shape. Therefore, in this study, a method is selected for analyzing only the corresponding region of the cross-sectional shape of one quarter as shown in Figure 2.

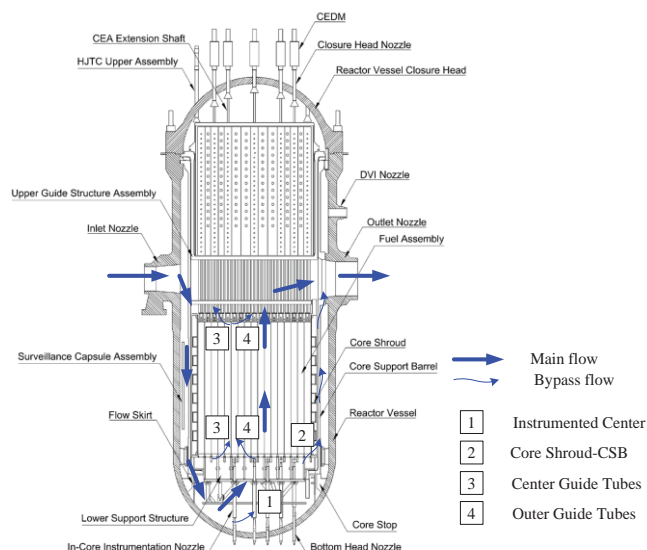


**Figure 1. General Arrangement and Flow Paths in the RV.**

## 2.2. Numerical Method

In the present computation, two-equation turbulence models are applied in this study considering efficiency and accuracy of the calculation, although there are various turbulence models such as one-equation models, large eddy simulation (LES), and Reynolds stress model (RSM). The  $k-\omega$  SST model is adopted at the stage of analysis which has several advantages, especially in the case of the near wall treatment for low-Reynolds number computations and is known to be excellent in accuracy and efficiency relative to two equation turbulence models. This model does not involve the complex non-linear damping functions required for the  $k-\epsilon$  model and is therefore more accurate and more robust. A near wall treatment that allows for a smooth shift from a low-Reynolds number form to a wall function formulation was applied. The main idea behind this formulation is to blend the wall value for  $\omega$  between the logarithmic and the near wall formulation. The flux for the  $k$ -equation is artificially kept at zero and the flux in the momentum equation is computed from the velocity profile. Due to the symmetry (in  $y$  and  $z$  directions) of the reactor vessel, only a quarter of the computational domain is finally used for the simulation.

The geometric modeling was divided into two parts; reactor core and internals (LSS, CS, CSB, Core upper part and cold/hot leg section). For the reactor core, a porous media model is adopted in the analysis because the actual shape of the reactor core is very complex and to create grid systems by applying a very complex core shape is a high cost problem. For the internals, the actual geometric dimensions of the APR1400 are used.

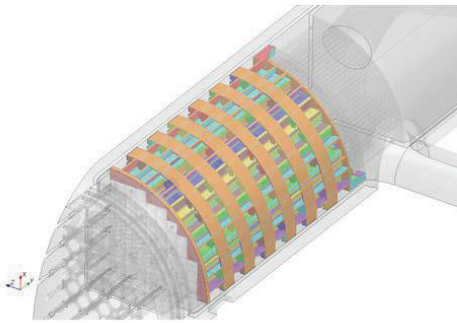


Figure 2. Geometric model of the RVI.

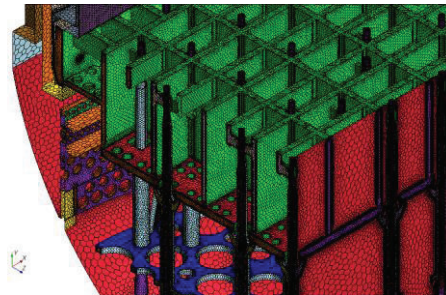


Figure 3. Computational grid.

The porous media method is commonly used to simulate the flow and heat transfer in large volume tube bundles. The flow passage is simplified as a channel flow governed by Darcy's law which relates the superficial velocity to the pressure gradient based on a measure of permeability. This law is given by the following equation.

$$-\nabla P = \frac{\mu}{k_p} v \quad (1)$$

In this equation,  $v$  is superficial velocity (m/s),  $\mu$  is viscosity ( $Pa \cdot s$ ), and  $k_p$  is permeability factor ( $m^2$ ). For the flow solver, porous source term appears in the momentum equation as tensor, so the above equation becomes:

$$f_p = -P \cdot v \quad (2)$$

$P$  is porous resistance tensor and given by the below equation.

$$P = P_v + P_i|v| \quad (3)$$

In this equation,  $P_v$  and  $P_i$  are the viscous (linear) and inertial (quadratic) resistance tensor, respectively. This equation is used to predict pressure drop for porous media in STAR-CCM+ commercial code[4]. With respect to the parameters of inertial resistance and viscous resistance in this model, the parameters for porous media are as follows.

$$Porosity = 1 - \frac{V_s}{V_T} \quad (4)$$

$V_T$  : Total volume including the solid and void components

$V_s$  : Volume of the solid

The effective thermal conductivity of the porous region is defined as the ratio of the open area to the total volume of the porous medium. This value is mainly used to mix the thermal conductivity of the solid and fluid materials[4].

$$\rho_s c_{p_s} (1 - \varepsilon) \frac{\partial \langle T \rangle^s}{\partial t} = k_s (1 - \varepsilon) \nabla^2 \langle T \rangle^s - \nabla \cdot \left[ \frac{1}{V} \int_s k_s T ds \right] - \frac{1}{V} \int_s k_s T ds \quad (5)$$

$$(\rho c_p)_{sf} = (1 - \varepsilon) \rho_s c_{p_s} + \varepsilon \rho_f c_{p_f} \quad (6)$$

$$k_{sf} = (1 - \varepsilon) k_s + \varepsilon k_f \quad (7)$$

$\varepsilon$  : porosity

$k_s$  and  $k_f$  : thermal conductivity of solid and fluid

### 2.3. Boundary Conditions and Simulation Parameters

The numerical study is analyzed in normal operation condition. The most important boundary condition is to reflect heat generation to the reactor core. The inflow coolant from the upper region is heated at the reactor core, which release heat of 995.75 MW that is the amount of heat generation from one quarter core model, and discharged through the outlet. As mentioned above, a thermal porous media methodology is used for the actual analysis for the reactor core. The working fluid is water, and the flow rate, operating pressure and thermal power are shown in Table I. The flow rate at the inlet flow of the reactor has a fully developed profile with a temperature of 290.6 °C and a pressure of 15.51 MPa in the RV and the water is discharged with a temperature of 323.9 °C under normal operation condition. The reactor outside is thermally shielded and there is no heat escape. Therefore, all of the outside walls were treated as adiabatic smooth walls obeying the no-slip conditions. The symmetry plane on both sides of a quarter model is adopted symmetry conditions. Inlet flow is applied at a flow rate condition of the pump discharge, which is divided into four equal parts in the 5,231.2 kg/s.

Table I. Design specifications of the reactor analysis

Grid test		Value	Unit
Thermal power		996	(MWt)
Operation pressure		15.51	(MPa)
Temperature	$T_{hot}$	323.9	°C
	$T_{cold}$	290.6	°C
Mass flow rate		5,231.2	Kg/s

Properties of water are calculated as a function of density and other thermodynamic factors in the International Association for the Properties of Water and Steam-Industrial Formulation 1997 (IPWS-IF97).

For irradiation condition, the neutron fluences and heat source to which RVI components are to be exposed during the reactor operation are calculated using the MCNP Code (Monte Carlo N-Particle transport code). MCNP calculations are performed for equilibrium fuel cycles. For the equilibrium fuel cycles, the different boron concentration stages of a fuel cycle which represent BOC, MOC, and EOC are considered for the calculation. Therefore, different axial power distributions are applied to each of BOC, MOC and EOC of the equilibrium fuel cycles. The sloping of the power densities in the axial direction reflects the nature of the ideal power distribution shape. Figure 4 illustrates the axial power and exposure distributions at the three points in core life with load sequence in fuel cycle during 60 years: beginning of cycle (BOC), middle of cycle (MOC) and end of cycle (EOC). The results of the different power density with fuel cycle are used as input data for the velocity and temperature distribution analysis on the each part of the RV.

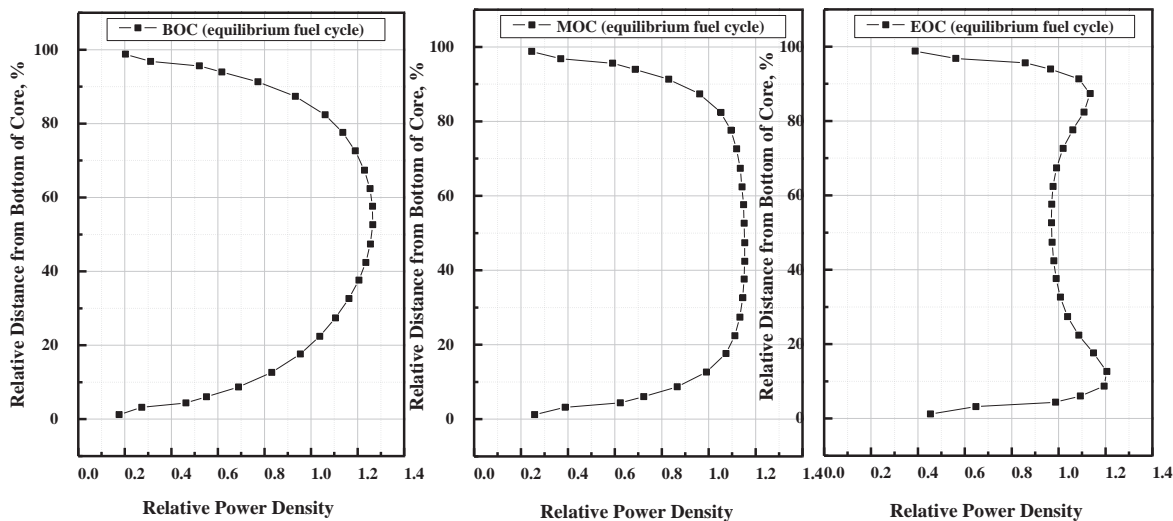


Figure 4. Axial Power Density Profile.

## 2.4. Mesh Generation and Grid Independency Analysis

The sensitivity grid for reactor analysis is examined in the present study. The polyhedral mesh provided by the STAR-CCM+ [4] is used and the mesh is generated, 27 million, 47 million and 67 million. The mesh configuration is shown in Figure 3. The appropriated grid size is determined by comparing the results of the pressure loss and temperature distribution in these three grid cases.

For the calculation of the pressure loss, the pressure is measured at the outlet and the inlet points of the reactor. The pressure loss in the grid test results is shown in Figure 5. As more number of cells are used, less pressure loss is calculated. However, comparing between mesh size 2 and 3, there is less than 1 % of difference of pressure drop. Therefore, mesh size 2 is selected for the CFD analysis considering the cost efficiency.

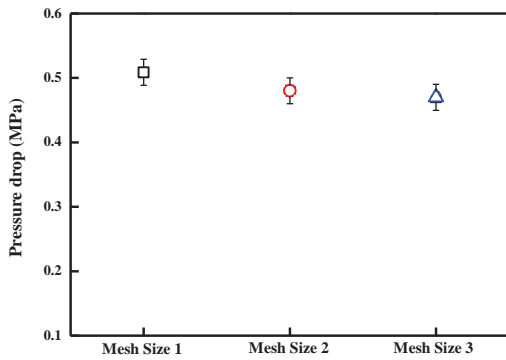


Figure 5. Pressure Drops in the grid test.

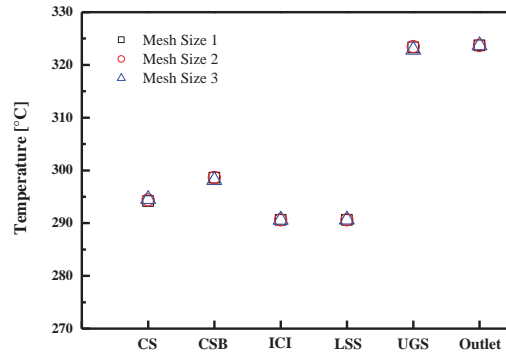


Figure 6. Average Temperatures in the grid test.

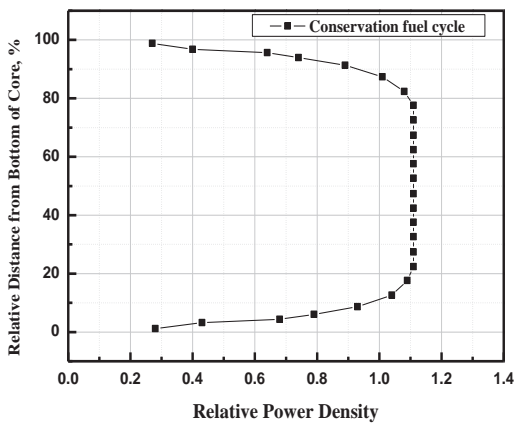


Figure 7. Axial Power Density Profile of Conservative Fuel Cycle

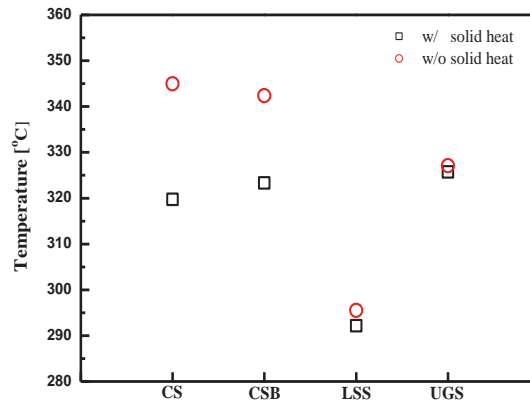


Figure 8. Maximum Temperature of Internal Structures

The average temperature distributions on the different parts of the RV are also compared to determine the grid size. As shown in Figure 6, significant differences of the average temperatures are measured among the RV parts because of relative distance from the heat source to the each part and the order of flow path. However, there are only few deviations of the average temperature in these three grid cases. The average temperature deviation corresponding to the number of grids is expected to result in a relatively uniform level (within 1% error) obtained by comparing those of the major components.

Although the pressure drops indicates small deviations in the three grid cases, there are just a few differences on the each parts of the RV. Therefore, the selected mesh resolution (47 million) would be appropriate to reproduce overall flow topology, and the mesh size 2 is adopted in this analysis considering the accuracy and efficiency of the calculation.

To investigate the effect of the irradiation heat with selected mesh resolution (47 million), conservative fuel cycle is considered for heat source as a representative case. The conservative axial power density is shown in Figure 7. The irradiation heat causes increasing the temperature of the internal structures. Particular, the CS shows the highest temperature and the largest difference of temperature comparing the analysis with irradiation heat and without irradiation heat in Figure 8. Actually, the difference of

maximum temperature of fluid in the RV between with irradiation and without irradiation is very small, that is about 0.01 °C.

The values of the heat sources CS, CSB, LSS and UGS are applied to the input values used in CFD considering structural heat generation.

## 2.5. Results and Discussion

### 2.5.1. CFD Analysis

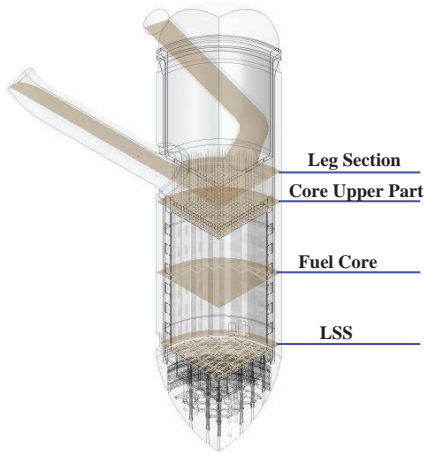


**Figure 9. Cross section of the one-quarter geometry.**

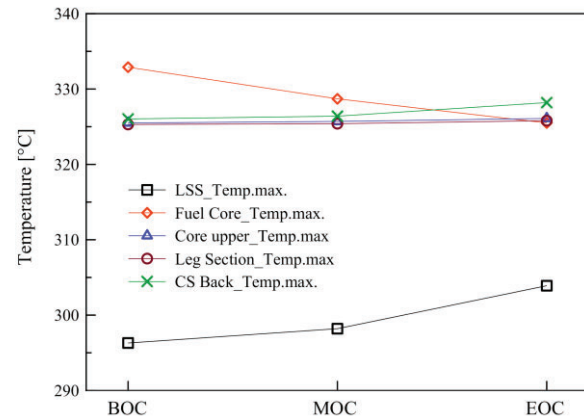


**Figure 10. Maximum temperature of the each cross section in the RVI.**

Each cross-section of four main parts of the RV in Figure 9 is selected for the calculation of the velocity and temperature distributions. The geometric range for radiation transport analysis is selected in the RVI components which would be expected to expose to the neutron fluence higher than  $5 \times 10^{19}$  n/cm<sup>2</sup>. However, to calculate the more accurate temperature data, the range for the CFD analysis is extended to include CSB, UGS support plate, RV shell and the parts of hot leg and cold leg which interfaces with structural analysis. The velocity and temperature distributions with different axial power density at the each cross-section are shown in Figure 11 and Figure 12.

Figure 11 shows the velocity distribution of the reactor internals. It seems no difference among the axial power density changes, BOC, MOC and EOC. The coolant velocity at the inlet (Figure 11 (a)) is developed and the flow rate is increased due to the thin gap between CSB and vessel and the flow path is where coolant is injected by pump. However, the velocity of the coolant becomes lower as the coolant comes down to the bottom of the reactor because the complex structures in the LSS interfere the flow. The velocity distributions at the inner side of the LSS (Figure 11 (d)) are uniform and slower, but the velocity between the CSB and the RV where the coolant flows down through cold leg is various and faster. This is because as the flow passes through the lower plenum region at the inner side of the LSS that consists of very complex and narrow structures, such as flow skirts, ICI and others, mixed flow is generated and making the flow relatively slow. Meanwhile, there is a simple and wide flow path between the CSB and the RV, and it allows the divers velocity distribution. Through the bundle of reactor core (Figure 11 (c)), the velocity is too low but the flow path from cold leg allows fast velocity. And through the UGS at the top (Figure 11 (b)), the flow velocity rapidly increases again via the narrow flow passage. The different power density does not have an effect on the velocity distributions.

On the contrary to the velocity distribution, the power density in each fuel cycle seems to have impact on the temperature distribution in Figure 12. It changes along with the axial power density variation. The maximum temperature on the LSS, core upper part and leg section (Figure 12 (a), (c), (d)) is increased, but the maximum temperature on the reactor core (Figure 12 (b)) is decreased. These are because of the axial power density changes. Although, the axial power density is increased on the bottom and top of the reactor core over time, the abrupt decrease of the maximum temperature is calculated on the reactor core.

Figure 12 (d) shows the temperature distributions in the cross section of the reactor bottom. Temperature distributions of the coolant are similar overall but the temperature differences of the LSS structure between the minimum and maximum values are relatively larger, BOC (290.6-296.2 °C), MOC (290.6-298.1 °C), EOC (290.6-303.6 °C)). As shown in Figure 12 (c), lower reactor temperature distributions are not relatively high. It is expected that the efficiency of cooling performance is good, because the cooling water flows continuously from the inflow of coolant at the inlet. Temperature distributions in the core upper part are shown in Figure 12 (b). Because flows of the reactor core and the internal inlet are separated by the outer wall, the temperature distributions at the top of the reactor core are displayed as relatively high while the temperature is low on the outer wall. Temperature distributions in the leg section of the reactor reactor core in Figure 12 (a) are at a very high level and about 326 °C, and it is substantially similar in all operating conditions. The temperature at the center of the reactor core is the highest, and it is relatively low on the outer wall by the coolant flow path.

The increase of the axial power density at around 0 % and 100 % of the relative distance from the bottom of the core through the BOC, the MOC and the EOC causes the higher temperature distributions on the LSS, Core Upper Part and Leg Section (Figure 10 and Figure 12 (a), (b) and (d)). However, the maximum temperature and the higher temperature area on the reactor core (Figure 10 and Figure 12 (c)) decreases and becomes smaller over time, the BOC through the EOC, as the axial power density between at around 20 % and 80 % of the relative height of the core is decreased in Figure 4.

The highest temperature is calculated on the reactor core at the BOC, where the neutron irradiation is utmostly concentrated on. The maximum temperatures on the reactor core at the BOC, MOC and EOC are 332.9 °C, 328.7 °C and 325.5 °C. Figure 13 shows temperature and isothermal distributions on the back and front sides of the CS which encloses reactor core. The area where the higher temperature distributes on the CS are identical to the results of MRP-230[2] which shows the area where the higher irradiation induced heat generation rate distributes on the CS. It is because the areas on the CS are located at the closest regions to the core, where the CS contacts vertically with the nuclear fuel.

### 3. CONCLUSIONS

The work presented in this study evaluates the velocity and temperature distributions in the RV considering a different power density of three fuel cycles: BOC, MOC and EOC.

First, Grid sensitivity analysis is performed with three sets of grids for efficient and economical calculation. To determine appropriate grid size for this study, pressure drops between the inlet and outlet of the RV and temperature distributions on several parts of the RV are compared. The relative differences of the pressure drops and temperature distributions in these three grid cases are less than 2 %. Considering standard deviation in the three grid cases, the 47 million mesh case is selected for the analysis . And the irradiation heat effect is investigated on the conservative fuel cycle condition with selected mesh. The structures are more influenced by the irradiation than fluid. And the highest temperature is calculated on the CS.

Second, with the different power density of three points of fuel cycle, velocity and temperature distributions are calculated on the four cross-sections of the RV: LSS, CS, upper part of the core and hot/cold leg center line. The different power density does not have an effect on the velocity distributions. However, temperature distributions change with each fuel cycle.

Through comparative analysis of RVI in APR 1400, the present study is performed in an attempt to establish a method for flow analysis of the reactor core using CFD. By the comparison of the results of grid tests of the APR1400 reactor, the cell size is determined without change of accuracy. This method established the effect of a variation of the flow according to BOC, MOC, EOC conditions. The results of each model show the similar patterns in the flow distributions, however the little difference appears in the temperature distributions under the operating conditions. The results of CFD analysis for the surface temperature distributions on the internals can be used for boundary conditions to perform stress analysis of the reactor vessel internals for the APR1400.

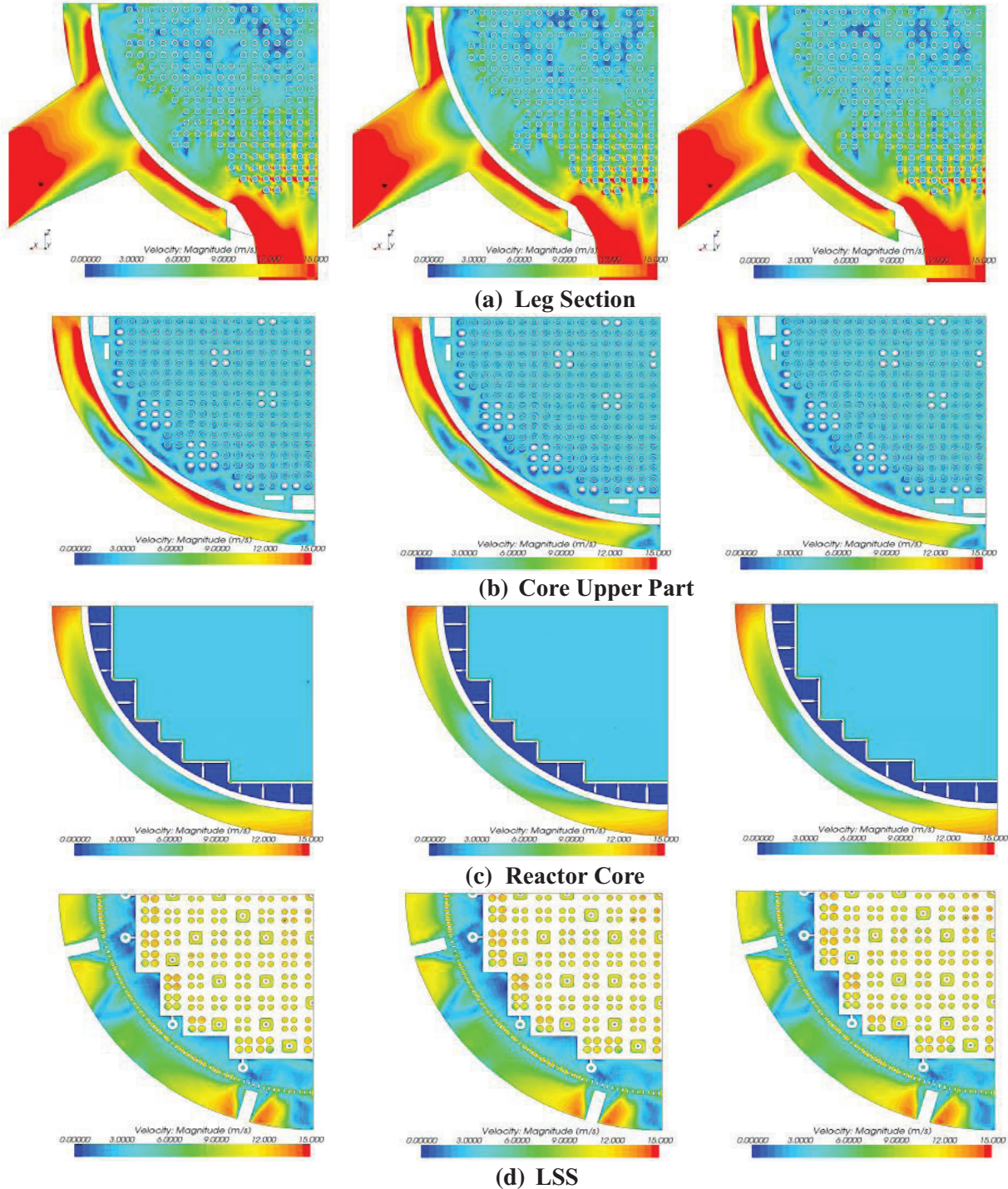
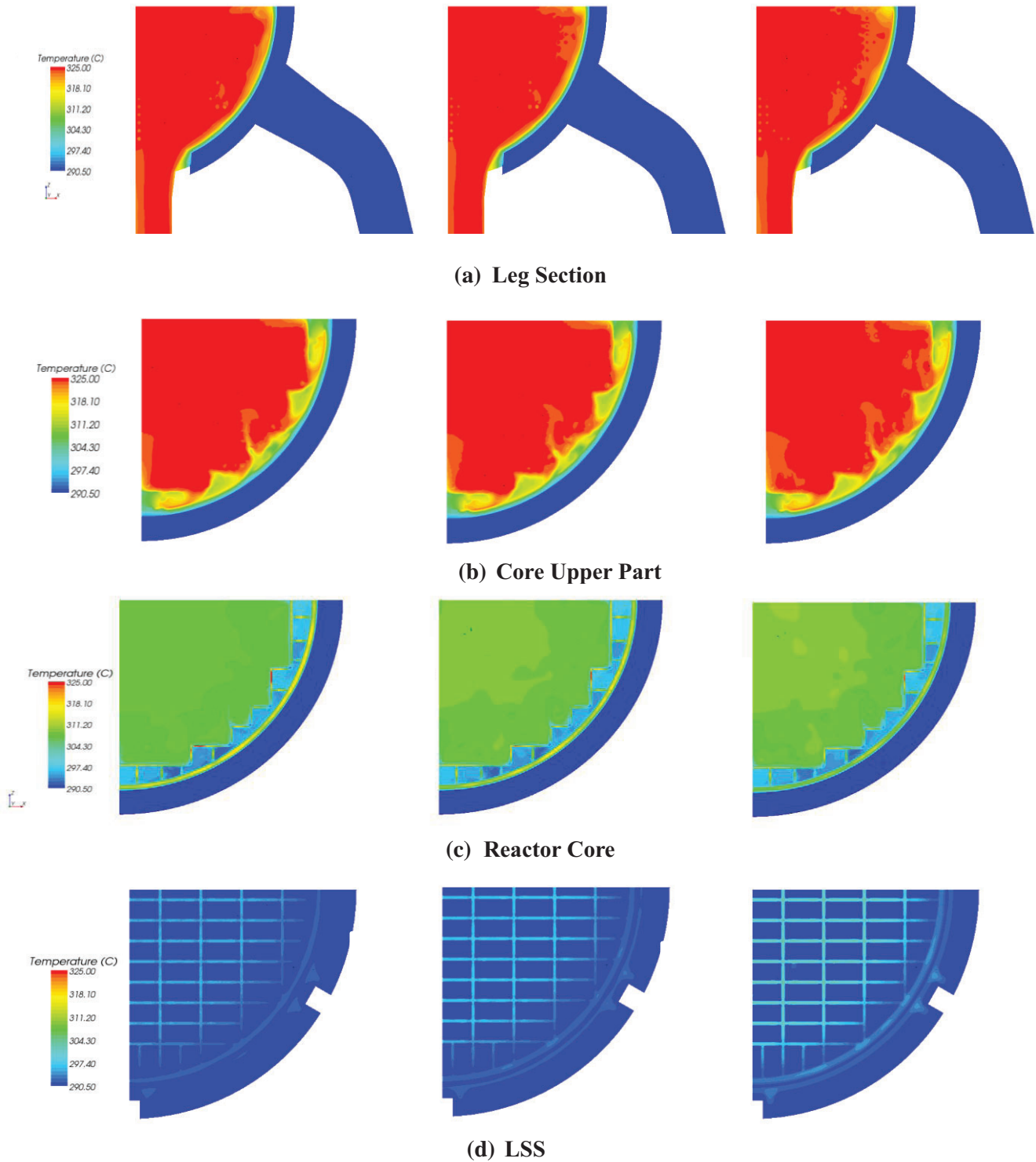
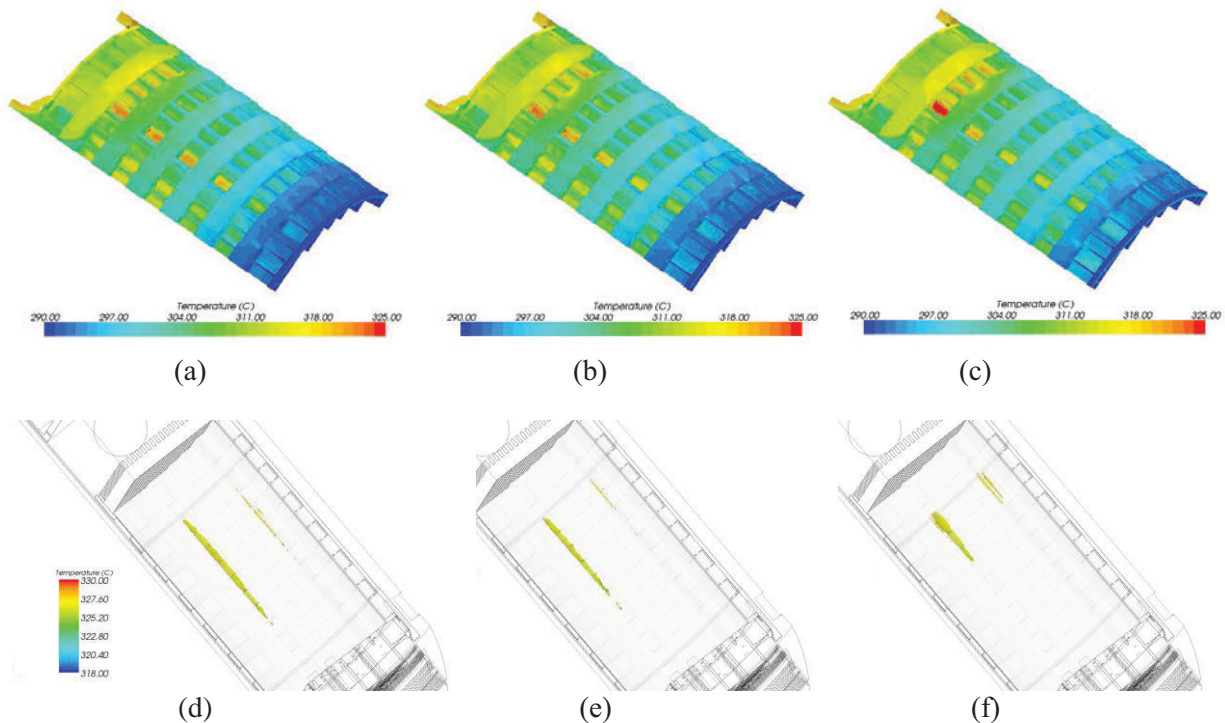


Figure 11. Velocity Distributions at Each Cross-Section.  
 (First Column : BOC, Second Column : MOC, Third Column : EOC).



**Figure 12. Temperature Distributions at Each Cross-Section.  
(First Column : BOC, Second Column : MOC, Third Column : EOC).**



**Figure 13. Temperature ((a), (b), (c)) and Isothermal ((d), (e), (f)) Distributions on the CS (First Column : BOC, Second Column : MOC, Third Column : EOC).**

#### NOMENCLATURE (IF NEEDED)

#### ACKNOWLEDGMENTS

#### REFERENCES

1. Materials Reliability Program: PWR Internals Material Aging Degradation Mechanism Screening and Threshold Values (MRP-175), EPRI, Palo Alto, CA: 2005. 1012081.
2. Materials Reliability Program: Functionality Analysis for Westinghouse and Combustion Engineering Representative PWR Internals (MRP-230, Revision 2), EPRI, Palo Alto, CA: 2012. 1021026
3. Was G.S., Atzmon M, Wang L, Busby J, "Mechanism of irradiation Assited Cracking of Core Components in Light Water Reactors", Final Report of Nuclear Engineering Educatoni Research(NEER) ( 2003)
4. "STAR-CCM+, Version 8.02 USER GUIDE," [www.cd-adapaco.com](http://www.cd-adapaco.com)
5. "MCNP – A General Monte Carlo N-Particle Transport Code Version 5", Los Alamos National Laboratory Vols. I-III ( April 2003 )